Travel Range Extension of a MEMS Electrostatic Microactuator

D. Piyabongkarn, Y. Sun, R. Rajamani, A. Sezen, and B. J. Nelson

***Abstract*—Electrostatic comb microactuators have had a fundamental limitation in that the allowable travel range is limited to one-third of the total gap between comb fingers. Travel beyond this allowable range results in "pull-in" instability, independent of mechanical design parameters such as stiffness and mass. This brief focuses on the development of an active control system that stabilizes the actuator and allows travel almost over the entire available gap between comb fingers. The challenges to be addressed include the nonlinear dynamics of the actuator and system parameters that vary with each fabricated device. A nonlinear model inversion technique is used to address the nonlinear dynamics of the system. An adaptive controller is developed to provide improved position tracking in the presence of fabrication imperfections. The developed control system is then implemented on a special microelectromechanical systems (MEMS) electrostatic microactuator fabricated using deep reactive ion etching (DRIE) on silicon-on- insulator (SOI) wafers. The use of DRIE allows the fabrication of a high aspect ratio device that can produce large electrostatic forces with low actuation voltages. Experimental results presented in the brief show that the resulting system is capable of traveling 4.0 μm over a 4.5 μm full range without "pull in." Good tracking performance is obtained over a wide frequency band. Potential applications of the actuator are in the manipulation of subcellular structures within biological cells, microassembly of hybrid MEMS devices, and manipulation of large molecules such as DNA or proteins.**

***Index Terms*—Electrostatic actuators, electrostatic positioning, nonlinear adaptive controller, pull-in effect, travel range extension.**

I. Introduction

ELECTROSTATICALLY ACTUATED devices are widely used in microelectromechanical systems (MEMS). The actuation principle behind parallel-plate electrostatic microactuators is the attractive force of two oppositely charged plates by applying a voltage between them. The comb-drive-type electrostatic microactuator has a large numbers of fine interdigitated "fingers" to generate the actuated force. A comb drive that is actuated by a parallel-plate field at each finger pair is called a "transverse" comb drive. The movable plate and movable finger are suspended by mechanical elastic members.

For transverse comb drive electrostatic microactuators, the electrostatic force is a nonlinear function of gap and the applied voltage. The electrostatic force has an inherent spring constant that is negative. The mechanical elastic members on the other hand provide a positive spring constant ensuring stability for small motion. Large motion is constrained by the fact that the electrostatic voltage that can be applied is limited by a specific value called "pull-in voltage." Electrostatic voltages over the pull-in voltage cause the negative electrostatic spring constant to exceed the elastic positive spring constant and makes the two parallel plates or comb fingers snap in together. The snap-in range is the so called "pull-in instability range" as illustrated in Fig. 1.

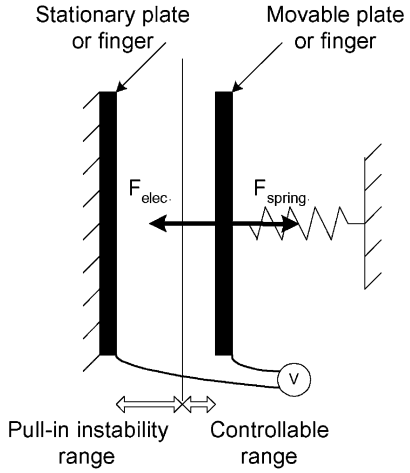

Fig. 1. Model of a parallel-plate or transverse comb drive electrostatic microactuator.

Pull-in instability limits the travel distance of elastically suspended parallel-plate and transverse comb drive microelectrostatic microactuators to approximately $1/3$ of the undeflected gap distance, as described in [1]–[7]. It is desirable to increase the controllable travel range of an electrostatic microactuator for applications that require high fill factors.

Several methods have been suggested to extend the controllable travel range, including the use of a multiphase piecewise linear mechanical flexure [1], by adding additional circuitry [2]–[4], by incorporating an onboard folded capacitor on the device [5], and by optimizing the structural design [6]. The use of an active control law was first proposed in [7] for an electrostatic actuator. However, its validity was not experimentally verified on fabricated devices. The first design and fabrication of a device with extended travel range was conducted by Chan *et al.* [5]. The travel range was extended from 0.3 to 0.6 μm out of a 1.0-μm total available gap. The scheme incorporated an onboard folded capacitor. The range extension was limited by the tilting instability caused by tether spring stiffness mismatches (which are intrinsic to folded parallel plate capacitors). While the device did succeed in extending the travel range, it still could not make use of a significant portion of the available gap. Another disadvantage of the developed device was that larger applied voltages were required for the same magnitude

Manuscript received September 16, 2002; revised July 1, 2003. Manuscript received in final form May 3, 2004. Recommended by Associate Editor A. Ray. This work was supported by the the National Science Foundation under Grant CMS-0116433.

D. Piyabongkarn, R. Rajamani, and A. Sezen are with the Department of Mechanical Engineering, University of Minnesota, Minneapolis, MN 55455 USA (e-mail: rajamani@me.umn.edu).

Y. Sun is with the Department of Mechanical and Industrial Engineering, University of Toronto, ON M5S 3G8, Canada.

B. J. Nelson is with the Institute of Robotics and Intelligent Systems, Swiss Federal Institute of Technology (ETH), CH-8092 Zurich, Switzerland (e-mail: brad.nelson@iris.mavt.ethz.ch).

Digital Object Identifier 10.1109/TCST.2004.838572

1063-6536/$20.00 © 2005 IEEE

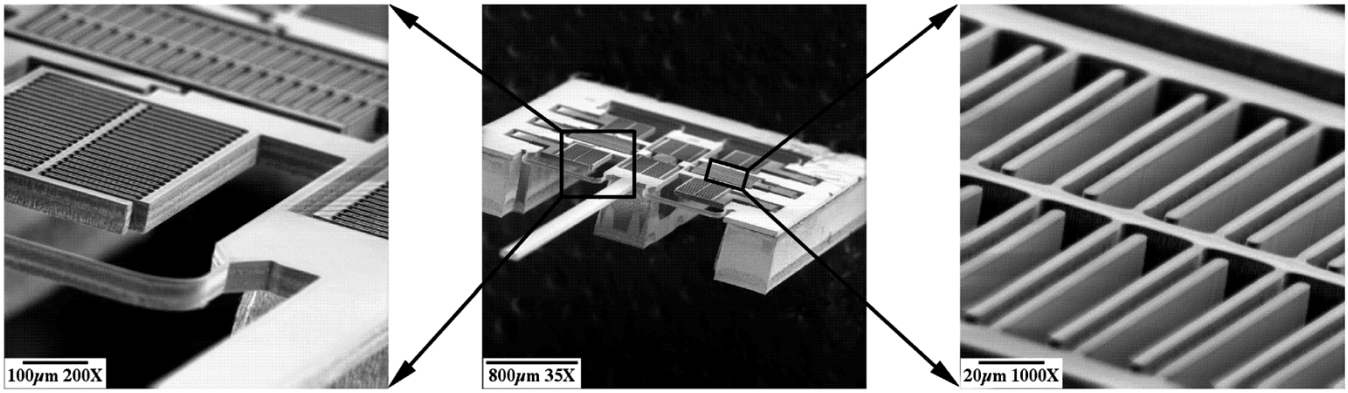

Fig. 2. Device scanning electron microscopy (SEM) micrograph.

of motion. The recent work done by Guardia *et al.* [12] presents a current-controlled method for extending the stable travel range. This method in effect is equivalent to charge control as described in [13]. Due to the inherent current leakage problem, the acutator's position beyond the pull-in point either cannot be maintained (stable only for a few seconds) or can be maintained only by constantly applying refresh current pulses and imposing stringent requirements on current sources' dynamic response.

This brief focuses on the development of an active control system that stabilizes the actuator and allows stable travel over the entire available gap between comb fingers. As will be described in the following sections, the challenges to be addressed in the design of the control system include the nonlinear dynamics of the actuator and system parameters that vary with each fabricated device. A nonlinear adaptive controller is developed to stabilize the system and provide accurate position tracking. The developed control system is then implemented on a special MEMS electrostatic microactuator fabricated using deep reactive ion etching (DRIE) on silicon-on-insulator (SOI) wafers. Experimental results on the performance obtained with the device under closed-loop control are presented.

II. Force Generation With Electrostatic Microactuators

A three-dimensional (3-D) high aspect ratio transverse comb drive microactuator shown in Fig. 2 was fabricated at the University of Minnesota, Minneapolis, using DRIE on SOI wafers. The term aspect ratio here refers to the ratio of depth to width of each comb finger. Due to the high aspect ratio, electrostatic forces that are two orders of magnitude larger than forces typically produced by surface micromachined lateral comb drives can be produced with actuation voltages approximately ten times smaller.

Fig. 3 shows a solid model of the microactuator. The constrained outer frame and the inner movable plate are connected by four curved springs. The device shown has six sets of comb fingers (six comb drives). When a voltage difference is applied on comb drive 1 and comb drive 4, the generated electrostatic force causes the movable plate to move in x, resulting in the movement of the manipulator for micromanipulation. This movement also changes the gap between each pair of the parallel plates of comb drive 3 and comb drive 6 causing a

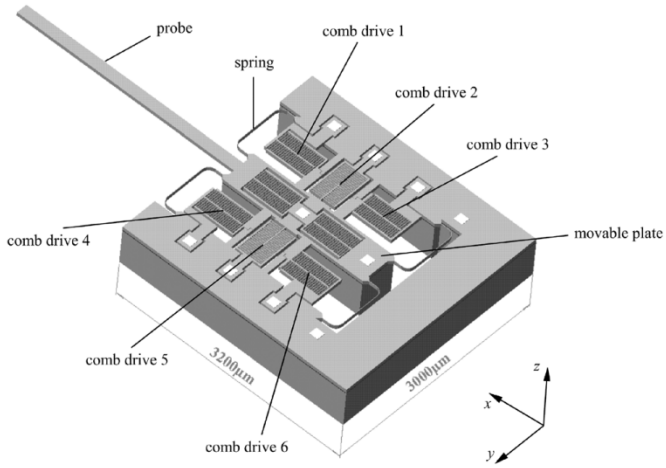

Fig. 3. Solid model of the two-axis microactuator.

capacitance change which is used to measure the actuation motion. To make the system capable of positioning in y, the interdigitated comb drive 2 and comb drive 5 are configured to be orthogonal to the comb drives in x.

Even though the fabricated microactuator has two-degrees-of-freedom (DOF), only the system in the x direction is utilized in this brief to study the travel range extension problem.

The one-axis comb drive model is shown in Fig. 4, where x is the displacement of the movable fingers from the equilibrium position. This comb drive is said to be "offset" since the distance x_1 is much smaller than the distance x_2. Each gap between adjacent fingers has a specific capacitance. For instance, C_1 and C_2 can be calculated by the following:

$$C_1 = \frac{K_d \varepsilon A}{x_1 - x} \quad \text{and} \quad C_2 = \frac{K_d \varepsilon A}{x_2 + x} \tag{1}$$

where K_d is the dielectric constant for the material (for air $K_d = 1$); $\varepsilon = 8.8542 \times 10^{-12}\ \mathrm{C}^2/(\mathrm{N} \times \mathrm{m}^2)$ is the permittivity of free space; $x_1 = 5\ \mu$m; $x_2 = 12\ \mu$m; and $A = 7500\ \mu\mathrm{m}^2$ is the overlapping area of each finger pair.

The total electrostatic force acting on the movable comb fingers is

$$F = N(F_1 - F_2) \tag{2}$$

$$F = \frac{1}{2} N \left[\frac{\partial C_1}{\partial (x_1 - x)} - \frac{\partial C_2}{\partial (x_2 + x)} \right] V^2 \tag{3}$$

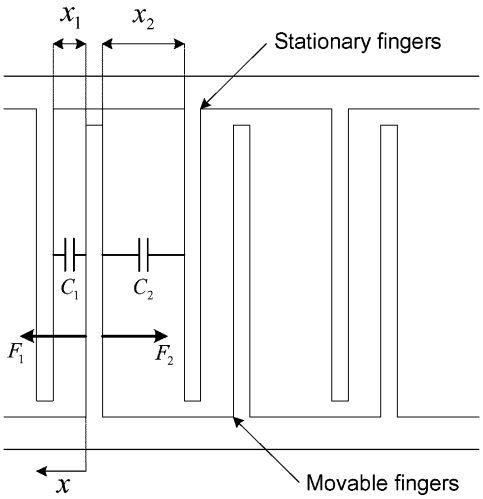

Fig. 4. Offset comb drive model.

where N is the number of parallel capacitor pairs and V is the applied actuation voltage. Hence, the electrostatic force equation is

$$F = \frac{1}{2}\mathrm{NK}_d \varepsilon A \left[\frac{(x_1+x_2)(x_2-x_1+2x)}{(x_1-x)^2(x_2+x)^2}\right] V^2. \quad (4)$$

Note that the above electrostatic force equation has some similarities with the actuator equation used in magnetic levitation. In magnetic levitation applications, the magnetic force varies as the square of the current and varies inversely with the square of the gap between the electromagnet and the reaction surface [14], [15].

The spring dimensions determine the mechanical stiffness of the system. The cantilever model can be used for calculating the force deflection relationships of the springs along both the x and y axes

$$\delta = \lambda \times \frac{F}{Et^3 h} \quad (5)$$

where δ is the deflection; F is the force acting on the springs; $E = 125$ GPa is the Young's modulus of silicon; $t = 7$ μm is the width of the springs; $h = 50$ μm is the height of the springs; $\lambda = 2.359 \times 10^{-10}$ m^3 in x, and $\lambda = 1.101 \times 10^{-11}$ m^3 in y. The spring stiffness along x and y were calculated to be 14.564 $\mu\mathrm{N}/\mu\mathrm{m}$ and 296.787 $\mu\mathrm{N}/\mu\mathrm{m}$, respectively. These values were also verified using ANSYS static simulations and later by experimental identification, as described in Section III.

III. System Identification

A. Experimental Setup

Fig. 5 shows a diagram of the overall real-time control system setup. The comb finger positions are measured using a capacitance readout circuit. The capacitance readout circuitry consists of a microcontroller and a capacitive readout ASIC, the MS3110 from MicroSensors with a resolution of 4.0 $\mathrm{aF}/\sqrt{\mathrm{Hz}}$. The Mathworks xPC-Target 1.3 is used to generate the real-time operating system kernel [8]. While the control software is written using Simulink on the host computer, the corresponding

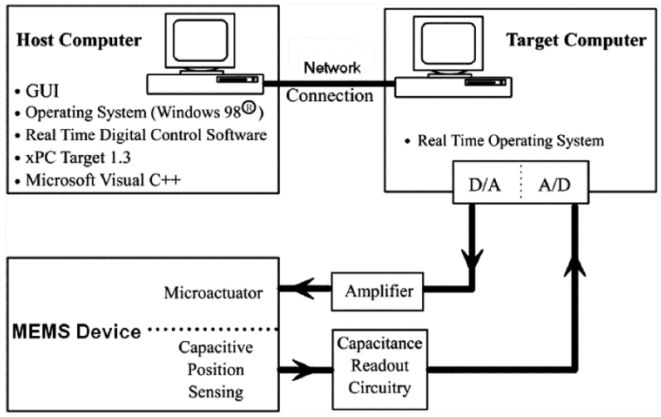

Fig. 5. Real-time control system setup.

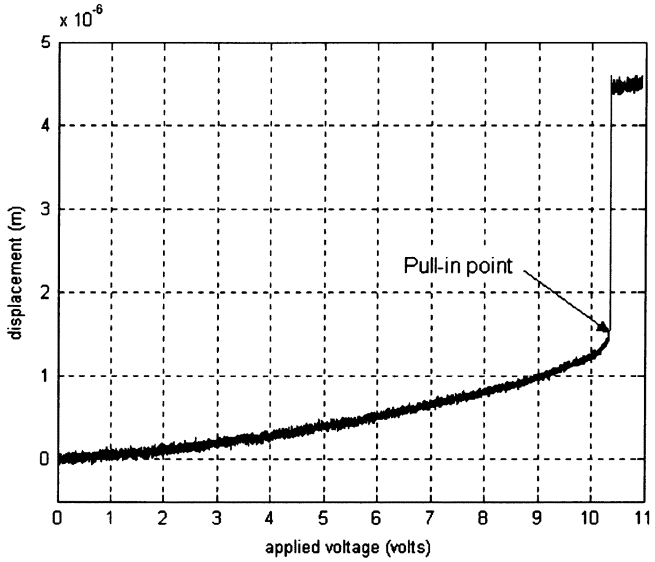

Fig. 6. Calibration of applied voltage and displacement.

real-time code is downloaded to the target computer through a network connection. A data acquisition card from National Instruments, PCI-MIO-16E-4, operates in the target computer and performs real-time sampling at a frequency of 20 kHz for this application.

B. System Modeling and Identification

The microactuator consisting of the movable and fixed comb fingers is modeled as a spring-mass-damper system. The equation of motion (EOM) is

$$m\ddot{x} + c\dot{x} + kx = F \quad (6)$$

where F is the electrostatic force exerted on the moving fingers by the applied voltage V, k is the mechanical stiffness, c is the mechanical viscous damping, and m the equivalent mass of the moving fingers.

Fig. 6 shows the relationship between applied open-loop voltages and the resulting actuator motion. In Fig. 6, when the applied voltage is greater than about 10.5 V, "pull-in" occurs at a displacement of 1.58 μ. Thus, the position of the comb fingers cannot be controlled beyond 1.58 μ using open-loop voltage

TABLE I
IDENTIFIED SYSTEM PARAMETERS

Parameters	*identified*	*analyzed*
mass (kg)	6.5×10^{-7}	6.58×10^{-7}
stiffness ($\mu N / \mu m$)	14.375	14.564
natural frequency (Hz)	748.46	748.76
damping ratio	[0.04,0.06]	-

commands. This pull-in behavior will be explained in more detail in Section IV. Though the total gap between the movable fingers and stationary fingers was designed to be 5 μm, the available gap is 4.5 μm because of an amplitude limit design that includes crash stops.

The mechanical stiffness of the system k was determined statically from the calibration results, and verified from the natural frequency of the system free response. The identified system stiffness of 14.375 N/m agrees well with the structural analysis results using ANSYS. The underdamped free response was also used to determine the damping ratio via the logarithmic decrement [9]. Table I shows the identified system parameters versus the parameters obtained from ANSYS.

IV. CONTROLLER DESIGN

A. Pull-In Analysis

The distance x traveled by the comb fingers for any applied constant voltage is determined by the elastic stiffness and the magnitude of the applied voltage. The equilibrium relationship is shown in the following equation and in Fig. 7:

$$kx = \frac{1}{2}\mathrm{N}\mathrm{K}_\varepsilon\varepsilon A\frac{(x_1+x_2)(x_2-x_1+2x)}{(x_1-x)^2(x_2+x)^2}V^2. \tag{7}$$

Fig. 7 shows that the spring force line F_s and many of the electrostatic force curves F_e intersect at two points. However, only the first of these two intersections points in each case is a stable equilibrium point. The other intersection point cannot be reached without increasing the applied voltage which means moving to a different F_e curve. The maximum distance that can be traveled and the corresponding voltage (x_e, V_e) can be determined by (7) and its partial derivative

$$\frac{\partial}{\partial x}(kx) = \frac{\partial}{\partial x}\left[\frac{1}{2}\mathrm{N}\mathrm{K}_d\varepsilon A\frac{(x_1+x_2)(x_2-x_1+2x)}{(x_1-x)^2(x_2+x)^2}V^2\right]. \tag{8}$$

At voltages below V_e, the system is stable and (7) can be applied. When a voltage larger than V_e is supplied, the electrostatic force is larger than the force that can be provided by the mechanical spring and the system becomes unstable. This voltage V_e is the so called "pull-in voltage." The maximum travel distance x_e is always 1.58 μm for the device tested or 31.6% of the undeflected gap of 5 μm, which can also be verified from the experimental results shown in Fig. 6. This pull-in distance is independent to the system stiffness and also slightly different from the traditional parallel-plate travel distance of $1/3$ of the gap because of different device configuration. The pull-in voltage $V_{\mathrm{pull-in}}$ is 10.34 V for our particular device stiffness of

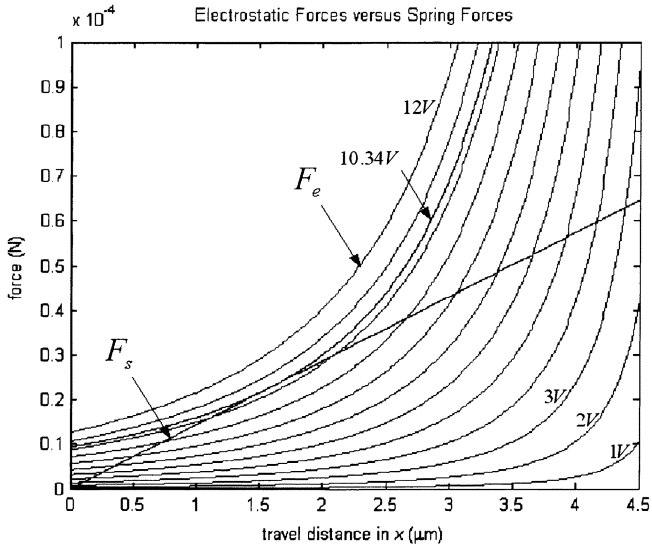

Fig. 7. Electrostatic force and spring force versus travel distance.

14.375 $\mu\mathrm{N}/\mu\mathrm{m}$. Obviously, the mechanical stiffness determines the pull-in voltage but the usable travel gap is, nonetheless, fixed at 1.58 μm independent of the stiffness value.

B. Nonlinear Model Inversion

A typical linear control law such as proportional derivative (PD) control can not directly be applied to the microactuator for tracking proposes beyond the pull-in limit (1.58 μm) because of high system nonlinearity. Implementing a linear feedback of position error is equivalent to electronically increasing the mechanical stiffness of the system. As we have seen, the electrostatic force is a nonlinear function of position, and its spring constant in the pull-in instability range will always exceed the mechanical spring constant and cause instability. A linear feedback law will, therefore, be inadequate. A nonlinear model inversion technique was used as shown in Fig. 8. The inverse nonlinear model is

$$V = f^{-1}(x_{\mathrm{meas}}, F_d) = \sqrt{\frac{2F_d(x_1-x_{\mathrm{meas}})^2(x_2+x_{\mathrm{meas}})^2}{\mathrm{N}\mathrm{K}_d\varepsilon A(x_1+x_2)(x_2-x_1+x_{\mathrm{meas}})}} \tag{9}$$

where x_{meas} is the position feedback; and F_d desired force. The desired force F_d can be determined from a linear controller.

Using this technique allows the use of traditional linear controller design methodologies for obtaining a desired linear system response. The nonlinearly compensated system can be considered as a second-order mass spring system, which is stable for the full travel range. For tracking control, the poorly damped poles of the open-loop system were cancelled by the zeros of the compensator. This was necessary in part because the position measurement circuit was very noisy and could not be differentiated to increase closed-loop damping. To make the loop transfer function behave as an integrator, a pole at zero and a pole at a higher frequency p were added to the compensator

$$\frac{F_d(s)}{E(s)} = K\frac{ms^2+cs+k}{s(s+p)} \tag{10}$$

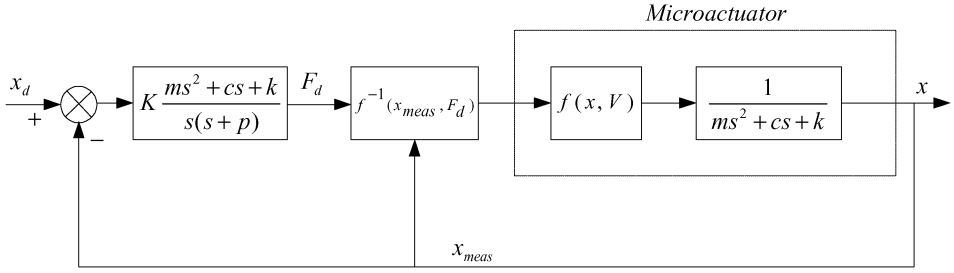

Fig. 8. Nonlinear model inversion position tracking.

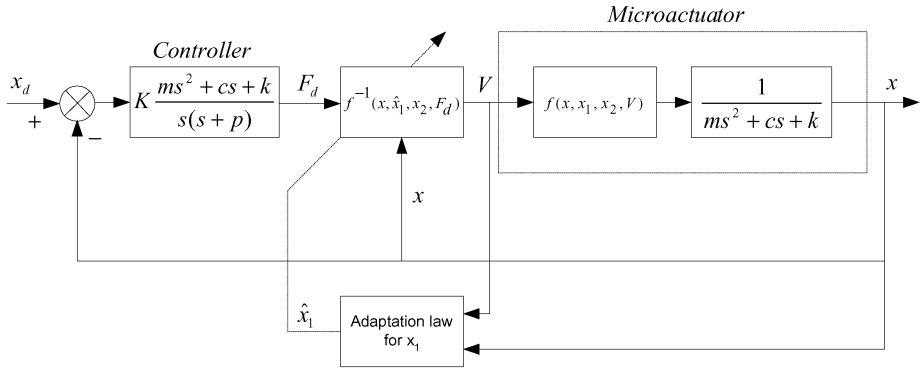

Fig. 9. Adaptive estimation for x_1.

where K is the overall control gain; and p represents a pole at high frequency.

The loop transfer function performs as an integrator in the low frequency range and has a cut-off frequency of K/p. The gain K can not be selected too high due to the presence of model uncertainty and noise. However, the proposed control law is less susceptible to noise than a direct application of PD control where it would be necessary to differentiate the position measurement. In addition, a PD controller could yield small steady-state error only if a very high bandwidth is used, which is not possible for the high-noise system.

V. Adaptive Parameter Estimation

Because the proposed control law is based on inversion of the nonlinear model, the accuracy of the model plays an important role. In the case of the MEMS comb actuator, the values of the parameters x_1 and x_2 vary significantly from device to device due to the inherent inaccuracies associated with bulk micromachining. The MEMS comb actuator is constructed from a number of comb pairs each of which can have different gap values because of fabrication imperfections. In the present device, the parameter x_1 has a nominal value of 5 μm while x_2 has a nominal value of 12 μm and is, therefore, much less important. Errors in x_1 have significantly greater impact on tracking and it is therefore important to have a good estimate of x_1 for each device. The mechanical constants m, c, and k can be quite accurately estimated from system identification and were therefore not considered for adaptation.

Adaptive online parameter estimation was developed to adapt on x_1 and to try and automatically compensate for device to device variations. The proposed tracking controller design is shown in Fig. 9.

From (4), the nonlinear model for the force can be rewritten as

$$F = f(x, x_1, V) = \gamma\phi(x, x_1)V^2 \tag{11}$$

where $\gamma = (1/2)\mathrm{NK}_d\varepsilon A, \phi(x, x_1) = ((x_1 + x_2)(x_2 - x_1 + 2x))/((x_1 - x)^2(x_2 + x)^2)$ and x_2 is constant. The equation of motion is

$$m\ddot{x} + c\dot{x} + kx = F. \tag{12}$$

The inverse nonlinear model is

$$f^{-1}(x, x_1, F_d) = \sqrt{\frac{F_d}{\gamma\phi(x, x_1)}}. \tag{13}$$

From the proposed control block diagram in Fig. 9, the desired force, F_d, from the controller can be written as

$$F_d = K\frac{ms^2 + cs + k}{s(s+p)}(x_d - x) \tag{14}$$

where x_d is the desired position. The high frequency pole is added in (14) to make the controller proper. It works as a first-order filter at high frequencies and the effect of the pole can be neglected at low frequencies.

Let the estimated parameter be $\hat{x}_1$ for the inverse nonlinear model or

$$V = f^{-1}(x, \hat{x}_1, F_d) = \sqrt{\frac{F_d}{\gamma\phi(x, \hat{x}_1)}}. \tag{15}$$

From (12)–(16), the dynamic equation can be written as

$$(ms^2 + cs + k)x = K\frac{\phi(x, x_1)}{\phi(x, \hat{x}_1)}\frac{ms^2 + cs + k}{s(s+p)}(x_d - x). \tag{16}$$

By letting $\tilde{x} = x - x_d$ and ignoring effect of the high frequency pole p in the right term, (16) can be written as

$$\dot{x} = -\frac{K}{p}\frac{\phi(x,x_1)}{\phi(x,\hat{x}_1)}\tilde{x}. \tag{17}$$

The following adaptation law is chosen for $\hat{x}_1$:

$$\dot{\hat{x}}_1 = \alpha e_f \tag{18}$$

where

$$e_f = \gamma\phi(x,\hat{x}_1)V^2 - \gamma\phi(x,x_1)V^2. \tag{19}$$

Due to the fact that x_1 is unknown and should not be used in (19), we used $m\ddot{x} + c\dot{x} + kx$ instead of $\gamma\phi(x,x_1)V^2$ in implementation. $\gamma\phi(x,x_1)V^2$ is actually equal to $m\ddot{x}+c\dot{x}+kx$ from (6). The term $\gamma\phi(x,x_1)V^2$ is used only for purposes of proving the theorem.

Theorem 1: If $\dot{x}_d$ is zero (i.e., if a constant desired position is being tracked), and the following assumptions are made:

1) $x \geq 0$;
2) $\hat{x}_1$ is set to have a sufficiently large initial value with a saturation function for the estimated value so that $\hat{x}_1 > x$ is always satisfied and, hence, $\hat{x}_1 > 0$;
3) A saturation limit is applied to $\hat{x}_1$ to make $\hat{x}_1 < x_2$. then $\tilde{x} \to 0$ as $t \to \infty$ if the adaptation law (18) and the control law (14) are used.

Proof: In the adaptive controller development, the assumption $x > 0$ is used because no repulsion can happen in the electrostatic actuation system being considered. x is always larger than 0. A saturation function is applied to $\hat{x}_1$ to ensure $\hat{x}_1 < x_2$. It makes physical sense to impose this constraint. The equilibrium values at zero voltage input to the moving comb fingers are such that $x_1 < x_2$ at equilibrium. Application of voltages to the moving comb fingers only reduces x_1 and increases x_2. Hence, the constraint $x_1 < x_2$ will hold for all voltage inputs.

We use Lyapunov theory to first show that the adaptive law ensures that the estimated error ($\tilde{x}_1 = \hat{x}_1 - x_1$) and tracking error ($\tilde{x} = x - x_d$) are bounded. Choose the Lyapunov function candidate for this system as

$$V = \frac{1}{2}\tilde{x}_1^2 + \frac{1}{2}\tilde{x}^2. \tag{20}$$

The time derivative of the Lyapunov function candidate is

$$\dot{V} = \tilde{x}_1\dot{\tilde{x}}_1 + \tilde{x}\dot{\tilde{x}}. \tag{21}$$

Substituting (17) into (21) yields

$$\dot{V} = \tilde{x}_1\dot{\tilde{x}} - \frac{K}{p}\frac{\phi(x,x_1)}{\phi(x,\hat{x}_1)}\tilde{x}^2 - \tilde{x}\dot{x}_d. \tag{22}$$

It can be shown as follows that the first term $\tilde{x}_1\dot{\tilde{x}}_1$ is always negative. By substituting (18) and (19) into $\tilde{x}_1\dot{\tilde{x}}_1$

$$\tilde{x}_1\dot{\tilde{x}}_1 = (\hat{x}_1 - x_1)[\phi(x,\hat{x}_1) - \phi(x,x_1)]\gamma V^2. \tag{23}$$

The next step is to prove that the function $\phi(x,\hat{x}_1)$ is a strictly decreasing function of the parameter $\hat{x}_1$. Hence, we need to prove that $(\partial\phi(x,\hat{x}_1))/(\partial\hat{x}_1)$ is always negative. Consider its derivative

$$\frac{\partial\phi(x,\hat{x}_1)}{\partial\hat{x}_1} = \frac{2}{(\hat{x}_1 - x)^3(x_2 + x)^2}\left[-x^2 - x_2^2 - 2x_2x\right]. \tag{24}$$

From the assumptions and from (24), it is clear that $(\partial\phi(x,\hat{x}_1))/(\partial\hat{x}_1)$ will be negative. This implies that the term $\tilde{x}_1\dot{\tilde{x}}_1$ will always be negative.

Next, consider the second term $(K/p)(\phi(x,x_1))/(\phi(x,\hat{x}_1))\tilde{x}^2$ and the last term $\tilde{x}\dot{x}_d$ in the case that $\dot{x}_d$ is not zero. With the assumptions 1, 2, and 3, $(\phi(x,x_1))/(\phi(x,\hat{x}_1))$ is always positive. If the error $\tilde{x}$ grows large enough so that

$$\frac{K}{p}\frac{\phi(x,x_1)}{\phi(x,\hat{x}_1)}\tilde{x}^2 \geq |\tilde{x}\dot{x}_d| \tag{25}$$

then the Lyapunov function derivative becomes negative semi-definite. This ensures that the estimation error is bounded by the following upper bound:

$$|\tilde{x}| \geq \frac{\phi(x,\hat{x}_1)}{\phi(x,x_1)}\frac{p}{K}|\dot{x}_d|. \tag{26}$$

By appropriate choice of K, this implies that the magnitude of $\tilde{x}$ can be bounded by a very small number $(\phi(x,\hat{x}_1))/(\phi(x,x_1))(p/K)|\dot{x}_d|$.

However, for the special case that $\dot{x}_d$ is zero, we can use Barbalat's lemma to show that $\lim_{t\to\infty}\tilde{x} = 0$.

From Barbalat's lemma: if $f(t) \in L_\infty \cap L_2$ and $\dot{f}(t) \in L_\infty$, then $\lim_{t\to\infty}f(t) = 0$.

If $\dot{x}_d$ is zero, then we have

$$\dot{V} = \tilde{x}_1\dot{\tilde{x}} - \frac{K}{p}\frac{\phi(x,x_1)}{\phi(x,\hat{x}_1)}\tilde{x}^2 \tag{27}$$

is negative semi-definite. Hence, $\tilde{x}_1(t)$ and $\tilde{x}(t)$ are only guaranteed to be bounded or $\tilde{x}_1, \tilde{x} \in L_\infty$.

Equation (18) can be rewritten as

$$\dot{\tilde{x}} = -\frac{K}{p}\frac{\phi(x,x_1)}{\phi(x,\hat{x}_1)}\tilde{x}. \tag{28}$$

Again, from the assumptions 1, 2, and 3, $(\phi(x,x_1))/(\phi(x,\hat{x}_1))$ is bounded when x and $\hat{x}_1$ are bounded. This implies that $\dot{\tilde{x}} \in L_\infty$.

Let $\tilde{x}_1\dot{\tilde{x}}_1 = V_1$, (27) can be rewritten as

$$\frac{K}{p}\frac{\phi(x,x_1)}{\phi(x,\hat{x}_1)}\tilde{x}^2 = V_1 - \dot{V}. \tag{29}$$

Due to the fact that V_1 is negative, therefore

$$\int_0^t \tilde{x}^2\,d\tau \leq -\frac{p}{K}\int_0^t \frac{\phi(x,\hat{x}_1)}{\phi(x,x_1)}\dot{V}\,d\tau. \tag{30}$$

Since $(\phi(x,\hat{x}_1))/(\phi(x,x_1))$ is bounded and $V(t)$ and $V(0)$ are bounded, this implies that $\int_0^t \tilde{x}^2 d\tau \in L_\infty$. Therefore $\tilde{x} \in L_2$.

Hence, from Barbalat's lemma, $\tilde{x} \to 0$ as $t \to \infty$.

VI. Experimental Results

Fig. 10 shows the sinusoidal tracking response of the experimental system without using adaptive parameter estimation. The parameter x_1 was simply set to be 5 μm in this case. The tracking response when adaptive parameter estimation is used for x_1 is shown in Fig. 11. A comparison of the tracking errors in both cases is shown in Fig. 12. The results clearly show that better tracking is ensured by using the adaptive estimation method. The steady-state error as well as the transient performance are improved.

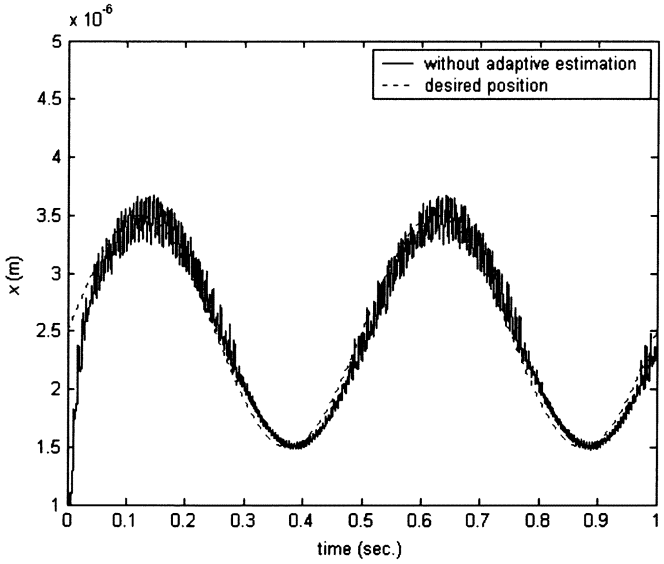

Fig. 10. Tracking without adaptive self-tuning controller.

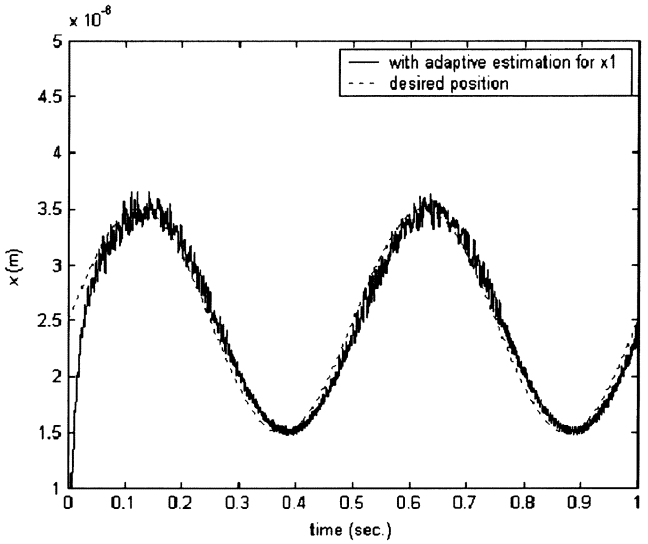

Fig. 11. Tracking with adaptive self-tuning controller.

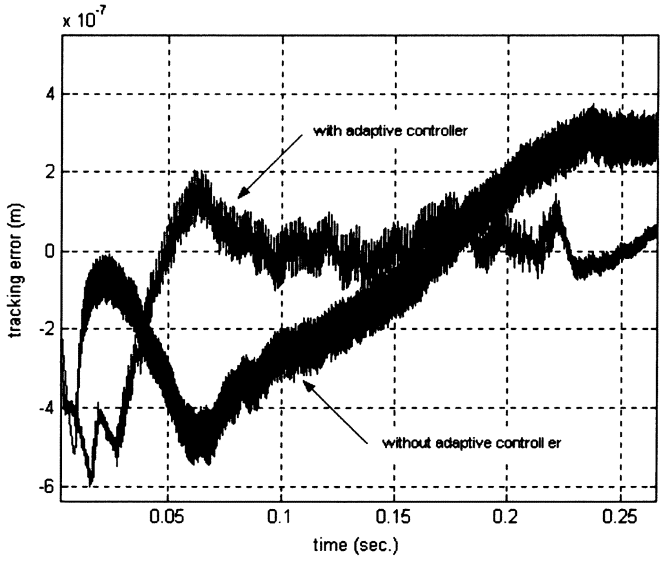

Fig. 12. Tracking errors with and without adaptive self-tuning controller.

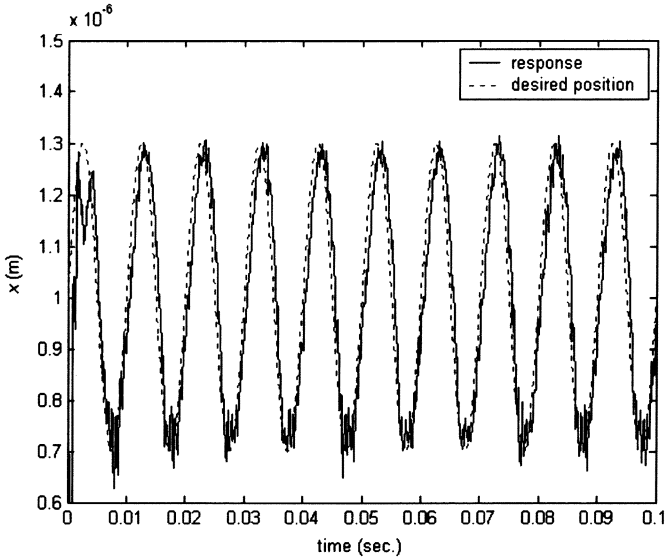

Fig. 13. 100 Hz sinusoidal tracking within $1/3$ of the gap.

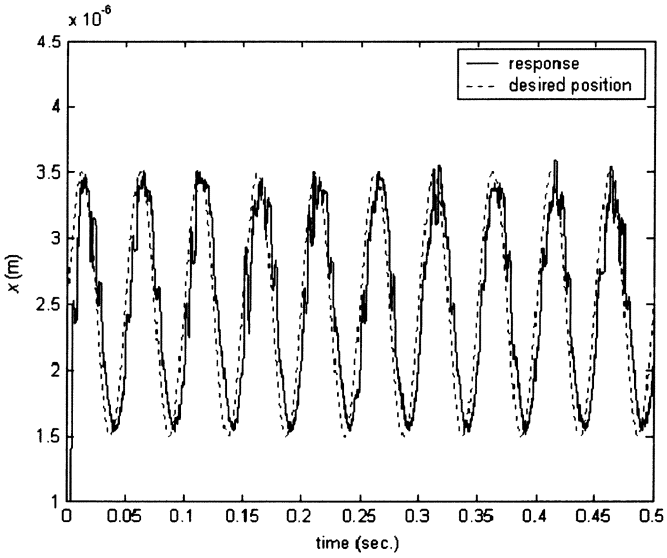

Fig. 14. 20 Hz sinusoidal tracking beyond $1/3$ of the gap.

The ability of the system to track a ramp was evaluated in order to find the maximum stable range of the system. The maximum stable range was found to be about 4 μm out of the available 4.5-μm full range. Thus, the travel range is increased to 80% of the gap, which means that the travel range is improved by 253% from the typical $1/3$ travel range of the gap.

The bandwidth of the closed-loop tracking that could be achieved was limited due to the signal-to-noise ratio being very low in the microactuator. A tracking bandwidth of 320 Hz in the stable 0–1.5 μm range and a tracking bandwidth of 20 Hz in the extended range (up to 4 μm) could be achieved. The sinusoidal tracking response of the system in the stable range and in the extended range is shown in Figs. 13 and 14, respectively.

VII. Conclusion

Historically, electrostatic comb microactuators have had a fundamental limitation in that the allowable travel range is always limited to one-third of the total gap between comb fingers. Travel beyond this allowable range results in "pull-in" in-

stability, independent of mechanical design parameters such as stiffness and mass. This brief focused on the development of an active control system that stabilized the actuator and allowed travel over the entire available gap between comb fingers. The challenges to be addressed included the nonlinear dynamics of the actuator, system parameters that varied with each fabricated device and difficulties in calibration of the position measurement circuit. A nonlinear adaptive controller was developed to stabilize the system and provide accurate position tracking. The developed control system was then implemented on a special MEMS electrostatic microactuator fabricated using DRIE on SOI wafers. The use of DRIE allowed the fabrication of a high aspect ratio device that can produce large electrostatic forces with low actuation voltage. Experimental results showed that the resulting system was capable of travelling 4.0 μm over a 4.5-μm full range without "pull in." Good tracking performance was obtained over a wide frequency band.

REFERENCES

[1] D. M. Burns and V. M. Bright, "Nonlinear flexure for stable deflection of an electrostatically actuated micromirror," *Proc. SPIE: Microelectronics Structures and MEMS for Optical Processing III*, vol. 3226, pp. 125–135, Sep. 1997.

[2] J. I. Seeger and S. B. Crary, "Stabilization of electrostatically actuated mechanical devices," in *Proc. Transducers'97*, Chicago, IL, pp. 1133–1136.

[3] ——, "Analysis and simulation of MOS capacitor feedback for stabilizing electrostatically actuated mechanical devices," in *Proc. Microsim II*, Boston, MA, 1998, pp. 199–208. Comput. Mech.

[4] J. I. Seeger and B. E. Boser, "Dynamics and control of parallel-plate actuators beyond the electrostatic instability," in *Proc. Transducers'99*, Sendai, Japan, pp. 474–477.

[5] E. K. Chan and R. W. Dutton, "Electrostatic micromechanical actuator with extended range of travel," *J. Microelectromech. Syst.*, vol. 9, no. 3, pp. 321–328, Sep. 2000.

[6] E. S. Hung and S. D. Senturia, "Extending the travel range of analog-tuned electrostatic actuators," *J. Microelectromech. Syst.*, vol. 8, no. 4, pp. 497–505, Dec. 1999.

[7] P. B. Chu and K. S. J. Pister, "Analysis of closed-loop control of parallel-plate electrostatic microgrippers," in *Proc. IEEE Conf. Robotics Automation*, San Diego, CA, May 1994, pp. 820–825.

[8] P. S. Shiakolas and D. Piyabongkarn, "On the development of a real-time digital control system using xPC-Target and a magnetic levitation device," in *Proc. 40th IEEE Conf. Decision Control*, Orlando, FL, Dec. 2001, pp. 1348–1353.

[9] W. J. Palm, *Modeling, Analysis, and Control of Dynamic Systems*. New York: Wiley, 2000.

[10] W. C. Tang, M. G. Lim, and R. T. Howe, "Electrostatic comb drive levitation and control method," *J. Microelectromech. Syst.*, vol. 1, no. 4, pp. 170–178, Dec. 1992.

[11] B. E. Boser and R. T. Howe, "Surface micromachined accelerometers," in *Proc. 1995 IEEE Custom Integrated Circuits Conf.*, vol. 31, Santa Clara, CA, May 1995, pp. 337–344.

[12] R. Nadal-Guardia, A. Dehé, R. Aigner, and L. M. Castaner, "Current drive methods to extend the range of travel of electrostatic microactuators beyond the voltage pull-in point," *J. Microelectromech. Syst.*, vol. 11, no. 3, Jun. 2002.

[13] S. D. Senturia, *Microsystem Design*. Norwell, MA: Kluwer, 2001.

[14] T. Namerikawa and M. Fujita, "Modeling and robustness analysis of a magnetic suspension system considering structured uncertainties," in *Proc. 36th Conf. Decision Control*, San Diego, CA, Dec. 1997, pp. 2559–2564.

[15] S. A. Green and K. C. Craig, "Robust, Digital, Nonlinear Control of Magnetic Levitation Systems," *ASME J. Dynam. Syst., Meas. Control*, vol. 120, pp. 488–495, Dec. 1998.